Numerical investigation of cooling effect on platinum nanoparticle formation in inductively coupled thermal plasmas

doi: 10.1063/1.2903918

Numerical investigation of cooling effect on platinum nanoparticle formation in inductively coupled thermal plasmas

Masaya Shigeta[1,a)] and Takayuki Watanabe[2,b)]
[1]*Department of Mechanical Systems and Design, Graduate School of Engineering, Tohoku University, 6-6-01 Aramaki-Aoba, Aoba-ku, Sendai 980-8579, Japan*
[2]*Department of Environmental Chemistry and Engineering, Interdisciplinary Graduate School of Science and Engineering, Tokyo Institute of Technology, 4259-G1-22 Nagatsuta, Midori-ku, Yokohama 226-8503, Japan*

(Received 30 November 2007; accepted 3 February 2008; published online 4 April 2008)

A mathematical model is developed to simulate the comprehensive systems of platinum nanoparticle synthesis using an argon inductively coupled thermal plasma flow with forced cooling portions. Numerical investigation using the model is conducted to clarify and discuss the effects of several cooling methods on the formation mechanisms of nanoparticles in distinctive thermofluid fields with strong two dimensionality. The computational results show that cooling by a radial gas injection, and a counterflow, engenders the remarkable promotion of nanoparticles. © *2008 American Institute of Physics*. [DOI: 10.1063/1.2903918]

I. INTRODUCTION

Efficient production of high-purity nanoparticles is necessary for myriad applications in industrial, biomedical, and environmental purification processes because nanoparticles exhibit unique capabilities such as electronic, optical, and catalytic properties, in addition to better hardness and ductility than those of larger particles of micrometer size or bulk materials.[1] Although several methods have been developed to produce nanoparticles, neither the precise control of the particle size nor mass production has been successful in practice. Even combustion processes cannot generate sufficiently high temperatures to vaporize the raw materials; furthermore, combustion requires an oxidation atmosphere, which is undesirable for the synthesis of metal nanoparticles and which engenders contamination from combustion products (CO_2, H_2O, etc.).

However, inductively coupled thermal plasma (ICTP) operated at atmospheric pressure has been anticipated as a potent tool for efficient production of nanoparticles[2–11] because an ICTP presents several distinctive advantages: high enthalpy, high chemical reactivity, variable properties, large plasma volume, and long residence/reaction time by virtue of its low velocity. Additionally, an ICTP is inherently contamination-free because it is generated without any internal electrodes. In such a field of plasma, a large amount of raw material, even that with a high melting/boiling point, is completely vaporized. Subsequently, the vapor is transported to the tail of an ICTP with a high cooling rate (10^4–10^5 K s^{-1}) and the vapor falls into a highly supersaturated state, which achieves effective formation of nanoparticles by nucleation and condensation. These processes progress continuously. Consequently, an ICTP can be regarded as an innovative tool that automatically creates nanoparticles with a high production rate.

It has been reported that nanoparticle formation is dramatically promoted by the forced cooling of the plasma flow with cold rings,[12] radial gas injection,[3,4,6] and counterflows.[13–15] Even though these cooling methods play important roles, their effects on the formation mechanisms of nanoparticles are still poorly understood. Nanoparticle formation in ICTPs with forced cooling is a remarkably severe and intricate heat/mass transfer process that involves phase conversion in a few milliseconds as well as interaction among the thermofluid field, the induced electromagnetic field, and the particle concentration field with numerous variables.[10] Therefore, the direct measurement and observation are practically arduous because of technical limitations, whereas theoretical/numerical studies require complicated mathematical formulation for its physics.

The objective of this study is to clarify the effects of several cooling methods on the formation mechanisms of nanoparticles in an ICTP using a numerical approach. First, a mathematical model is developed to simulate the comprehensive systems for nanoparticle synthesis by an ICTP with cooling portions. The thermofluid field in the ICTP is expressed based on the electromagnetic fluid dynamics. The trajectory and temperature history of the precursory powders are examined using a Lagrangian approach, taking into account the rarefied gas effects; thereby, the vapor production field in the ICTP is obtained. The nanoparticle formation is modeled by the aerosol dynamics, taking into account not only nucleation, condensation, and coagulation but also convection, diffusion, and thermophoresis because the nanoparticles will form a spatial distribution with a considerable two dimensionality because of the intriguing thermofluid field of the plasma flow with cooling.

In this study, synthesis of platinum nanoparticles by an argon ICTP is particularly selected because it is significant to clarify the formation mechanism of platinum nanoparticles, which are expected to be used for automobile exhaust catalysts,[16] fuel cells,[17] and so on. Platinum nanoparticles provide a very large specific surface area because of their very small size. For that reason, the catalytic properties and reactivity are tremendously enhanced. Furthermore, this pro-

a)Tel.: +81-22-795-6929. FAX: +81-22-795-6927. Electronic mail: shigeta@fluid.mech.tohoku.ac.jp.
b)Tel.: +81-45-924-5414. FAX: +81-45-924-5414.

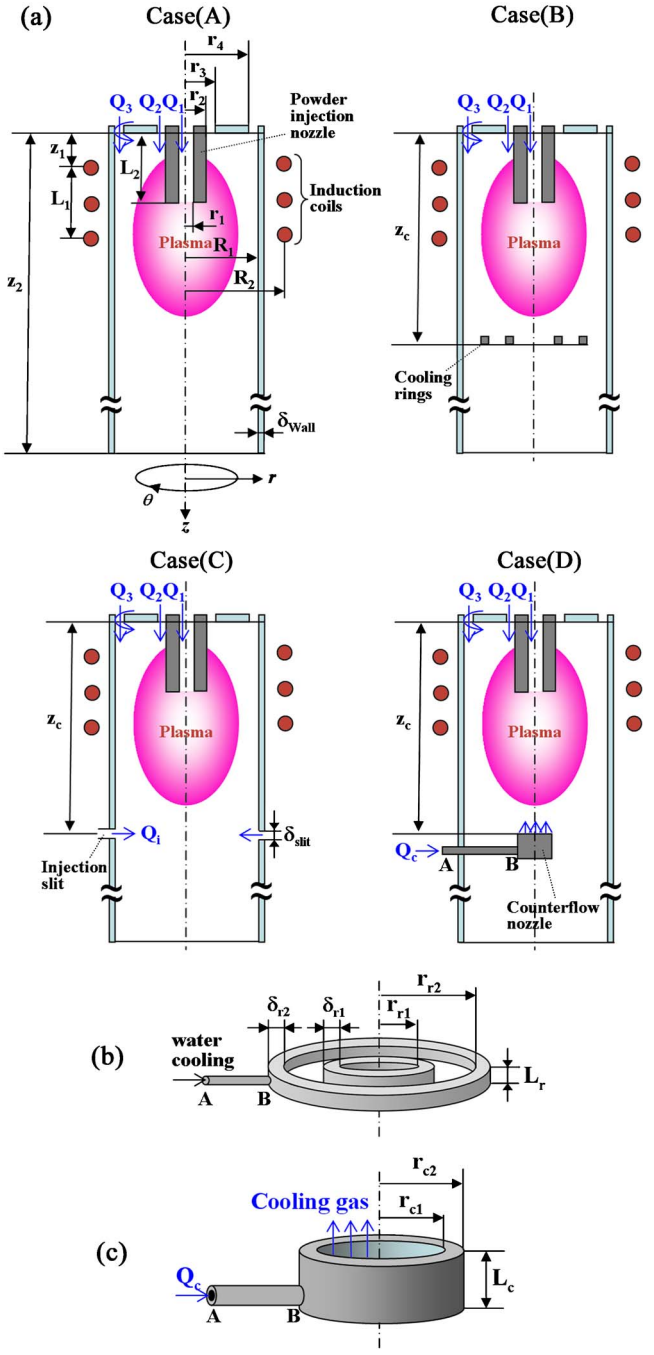

FIG. 1. (Color online) Schematic of nanoparticle synthesis systems: (a) Case A: conventional ICTP torch; case B: ICTP torch with cooling rings; case C: ICTP torch with radial cooling gas injection; and case D: ICTP torch with counterflow cooling; (b) cooling rings for case B; (c) counterflow nozzle for case D.

cess includes chemical reactions that might cause a problem, which makes it possible to specifically examine the physics. Finally, the validity of this model is discussed.

II. MODEL DESCRIPTION

A. Geometry and operating conditions of nanoparticle synthesis systems

Figure 1(a) depicts schematic illustrations of ICTP systems to synthesize nanoparticles. Cases B–D have typical cooling portions to promote nanoparticle formation. In case B, two water-cooled rings, as presented in Fig. 1(b), are installed in the downstream region from the ICTP torch region. Case C has a slit for the radial injection of cooling gas. In case D, a counterflow nozzle is set up for head-on quenching against the plasma flow, as presented in Fig. 1(c). The geometries and operating conditions are presented in Table I. The ICTP torch wall is a quartz cylinder. Its outer surface is water cooled to be 300 K. The induction coil consists of three turns and applies the actual power of 3.0 kW and the induction frequency of 4.0 MHz to the plasma. Argon gas is injected as the carrier gas (1.0 Sl min^{-1}), the plasma supporting gas (1.0 Sl min^{-1}), and the sheath gas (10.0 Sl min^{-1}) with 300 K. The sheath gas has not only an axial velocity but also an azimuthal velocity to stabilize the plasma flow. The precursory powders of platinum are supplied (0.1 g min^{-1}) with the carrier gas from the powder injection nozzle, which is regarded as a dilute condition.

TABLE I. Geometry and operating conditions.

Inner radius of powder injection nozzle (r_1)	1.0 mm
Outer radius of powder injection nozzle (r_2)	4.5 mm
Outer radius of inner slot (r_3)	6.5 mm
Inner radius of outer slot (r_4)	21.0 mm
Inner radius of torch (R_1)	22.5 mm
Radius of induction coils (R_2)	32.0 mm
Distance to front end of coil (z_1)	19.0 mm
Length of coil (L_1)	46.0 mm
Insertion length of probe (L_2)	45.0 mm
Torch length (z_2)	600.0 mm
Actual input power	3.0 kW
Induction frequency	4.0 MHz
Coil turn number	3
Operating pressure	101.3 kPa
Wall thickness (δ_W)	1.5 mm
Flow rate of career gas (Q_1)	1.0 Sl min^{-1}
Flow rate of plasma gas (Q_2)	1.0 Sl min^{-1}
Flow rate of sheath gas (Q_3)	10.0 Sl min^{-1}
Feed rate of precursory powders	0.1 g min^{-1}
Axial position of cooling units (z_c)	200.0 mm
Temperature of cooling units	300.0 K
Inner radius of inner cooling ring (r_{r1})	5.5 mm
Inner radius of outer cooling ring (r_{r2})	14.0 mm
Width of inner cooling ring (δ_{r1})	1.0 mm
Width of outer cooling ring (δ_{r2})	1.0 mm
Thickness of cooling rings (L_r)	1.0 mm
Width of injection slit (δ_{slit})	1.0 mm
Flow rate of radial injection (Q_i)	15.0 Sl min^{-1}
Inner radius of counterflow nozzle (r_{c1})	5.0 mm
Outer radius of counterflow nozzle (r_{c2})	6.0 mm
Length of counterflow nozzle (L_c)	10.0 mm
Flow rate of counterflow (Q_c)	6.0 Sl min^{-1}
Cooling gas temperature	300.0 K

The platinum powders evaporate because of the high enthalpy of the ICTP. The vapor is transported downstream with the plasma flow. The saturation pressure drastically decreases with the rapid temperature drop at the tail of the plasma. Therefore, the vapor falls into a supersaturated state. Consequently, nuclei are generated by homogeneous nucleation. The supersaturated vapor readily condenses on the nuclei through heterogeneous condensation. This process is

known as the fundamental formation mechanism of nanoparticles. Simultaneously, nanoparticles collide and coagulate among themselves. Coagulation also plays an important role for nanoparticle growth.

In this study, tube AB in Figs. 1(b) and 1(c) is ideally neglected because its thickness is assumed to be sufficiently small. All processes are operated at atmospheric pressure in a two-dimensional axisymmetric system with axial coordinate z and radial coordinate r.

B. ICTP flow model

The flow of ICTP is determined using the electromagnetic fluid dynamics approach. To derive the governing equations, several assumptions are introduced: (i) steady-state laminar flow; (ii) optically thin; (iii) negligible viscous dissipation; (iv) negligible displacement current; (v) negligible flow-induced electromagnetic field; (vi) identical temperatures of argon atoms, argon ions, and electrons; (vii) negligible effect of platinum vapor/particles on thermofluid fields/properties of the plasma flow because of a dilute condition. The governing equations of the thermofluid field such as velocity and temperature fields are expressed as conservation laws.

The plasma flow satisfies the continuity condition, i.e., the conservation of mass,

$$\frac{\partial}{\partial z}(\rho u_z) + \frac{1}{r}\frac{\partial}{\partial r}(r\rho u_r) = 0, \tag{1}$$

where ρ is the fluid density and u is the velocity component. Subscripts z and r, respectively, represent the axial and the radial components.

The velocity field is obtained by solving the equations of momentum conservation for the three components (axial component)

$$\frac{\partial}{\partial z}(\rho u_z u_z) + \frac{1}{r}\frac{\partial}{\partial r}(r\rho u_z u_r) = -\frac{\partial p}{\partial z} + 2\frac{\partial}{\partial z}\left(\eta\frac{\partial u_z}{\partial z}\right) + \frac{1}{r}\frac{\partial}{\partial r}\left[r\eta\left(\frac{\partial u_z}{\partial r} + \frac{\partial u_r}{\partial z}\right)\right] - \frac{2}{3}\frac{\partial}{\partial z}\left\{\eta\left[\frac{\partial u_z}{\partial z} + \frac{1}{r}\frac{\partial (ru_r)}{\partial r}\right]\right\} + F_z, \tag{2}$$

(radial component)

$$\frac{\partial}{\partial z}(\rho u_r u_z) + \frac{1}{r}\frac{\partial}{\partial r}(r\rho u_r u_r) = -\frac{\partial p}{\partial r} + \frac{\partial}{\partial z}\left[\eta\left(\frac{\partial u_r}{\partial z} + \frac{\partial u_z}{\partial r}\right)\right] + \frac{2}{r}\frac{\partial}{\partial r}\left(r\eta\frac{\partial u_r}{\partial r}\right) - \frac{2}{3}\frac{\partial}{\partial r}\left\{\eta\left[\frac{\partial u_z}{\partial z} + \frac{1}{r}\frac{\partial (ru_r)}{\partial r}\right]\right\} - \eta\frac{2u_r}{r^2} + \rho\frac{u_\theta^2}{r} + F_r, \tag{3}$$

(azimuthal component)

$$\frac{\partial}{\partial z}(\rho u_\theta u_z) + \frac{1}{r}\frac{\partial}{\partial r}(r\rho u_\theta u_r) = \frac{\partial}{\partial z}\left(\eta\frac{\partial u_\theta}{\partial z}\right) + \frac{1}{r}\frac{\partial}{\partial r}\left(r\eta\frac{\partial u_\theta}{\partial r}\right) - \eta\frac{u_\theta}{r^2}\frac{\partial}{\partial r}(r\eta) - \rho\frac{u_r u_\theta}{r}. \tag{4}$$

In those equations, p is the pressure and η is the viscosity. Subscript θ denotes the azimuthal component. Also, F represents the component of the Lorentz force that is generated by the electromagnetic field induced in the plasma flow and which is estimated as the following time-averaged values:

$$F_z = -\tfrac{1}{2}\sigma_e \,\mathrm{Real}(E_\theta \tilde{B}_r), \tag{5}$$

$$F_r = \tfrac{1}{2}\sigma_e \,\mathrm{Real}(E_\theta \tilde{B}_z). \tag{6}$$

Therein, σ_e is the electrical conductivity. In addition, E and B, respectively, denote the components of the electric field and the magnetic flux density. The auxiliary symbol $\sim$ denotes the complex conjugate.

The energy of the plasma flow is balanced with the generation by Joule heating, the loss by radiation, the transport by convection, and the diffusion by thermal conduction.

$$\frac{\partial}{\partial z}(\rho h u_z) + \frac{1}{r}\frac{\partial}{\partial r}(\rho h u_r) = \frac{\partial}{\partial z}\left(\frac{\lambda}{C_p}\frac{\partial h}{\partial z}\right) + \frac{1}{r}\frac{\partial}{\partial r}\left(r\frac{\lambda}{C_p}\frac{\partial h}{\partial r}\right) + \dot{Q}_{\mathrm{Joule}} - \dot{Q}_{\mathrm{rad}}. \tag{7}$$

In that equation, h is the enthalpy, λ is the thermal conductivity, and C_p is the specific heat at constant pressure. Also, $\dot{Q}_{\mathrm{Joule}}$ represents the Joule heating estimated as

$$\dot{Q}_{\mathrm{Joule}} = \tfrac{1}{2}\sigma_e(E_\theta \tilde{E}_\theta). \tag{8}$$

In addition, $\dot{Q}_{\mathrm{rad}}$ denotes the radiation loss. The plasma losses its energy by radiation because of its intensive light emission. In many cases of fluid mechanics, viscous dissipation contributes to heat generation. However, it is estimated to be about 250 W m^{-3} even in a zone with a steep velocity gradient. On the other hand, because Joule heating generates energy on the order of 10^8 W m^{-3}, the viscous dissipation is negligible. The effect of the enthalpy transport attributable to species diffusion also plays an important role for compressible flows. An ICTP, however, is generally considered as an incompressible flow because it has low Reynolds and Mach numbers because of its inherent low velocity under atmospheric pressure. The temperature of a thermal plasma increases to more than 9000 K with the increases in the viscosity and with the decrease in the density. Consequently, the Reynolds number is estimated to be, at most, in the order of 10^2 with the torch diameter as a reference length. Additionally, the acoustic sound increases to approximately 1800 m s^{-1}. For that reason, the Mach number is estimated to be 0.01 at most. An ICTP is therefore an incompressible flow, and the effect of the enthalpy transport attributable to species diffusion is negligible. The density depends on the temperature, but is not affected by the flow compressibility.

The ICTP is maintained using the effect of the electromagnetic field induced in the plasma itself. Therefore, the electromagnetic field must also be determined to obtain the

profile of the ICTP flow. The electromagnetic field induced in the plasma is expressed as the vector potential from Maxwell's equations as

$$\frac{\partial^2 A_\theta}{\partial z^2} + \frac{1}{r}\frac{\partial}{\partial r}\left(r\frac{\partial A_\theta}{\partial r}\right) - \frac{A_\theta}{r^2} = i\mu_0\sigma_e\omega A_\theta, \tag{9}$$

where A represents the vector potential, μ_0 is the permeability in vacuum, and ω is the angular frequency. Actually, i denotes $\sqrt{-1}$. This equation is divided into the real part and the imaginary part and is then solved simultaneously.[18] For a standard geometry of an ICTP torch, the electric field induced in the plasma, and therefore the vector potential, can be assumed to have only an azimuthal component. The induced electric field and magnetic fields are, consequently, obtained from the vector potential,

$$E_\theta = -i\omega A_\theta, \tag{10}$$

$$B_z = \frac{1}{r}\frac{\partial(rA_\theta)}{\partial r}, \tag{11}$$

$$B_r = -\frac{\partial A_\theta}{\partial z}. \tag{12}$$

The boundary conditions for the thermofluid field and the induced electromagnetic field were, respectively, similar to those described in earlier studies (Refs. 19 and 18). At the wall, the nonslip condition was given for the flow field. Then heat conduction from the plasma to the outside of the torch was considered to determine the wall temperature. For the induced electromagnetic field, the effects not only of the induction coils but also of the electric current induced in the plasma were considered and given on the wall using complete elliptic integrals. On the central axis and at the exit, the Neumann condition was given to all the variables. These boundary conditions depend strongly on the plasma profile. Therefore, they were updated in every iteration step until convergence.

The transport properties such as the viscosity, the thermal conductivity, the electrical conductivity, and the heat capacity have considerable dependence on the temperature and the concentration of the plasma species. Therefore, for use in this study, these properties were obtained from our previous work[19] based on the Chapman–Enskog method.[20] The radiation loss was estimated as in Ref. 21.

The computational domain, respectively, was discretized into the nonuniform staggered-grid system of 347 and 47 in the axial and radial directions. The governing equations were solved using semiimplicit method for pressure linked equation revised (SIMPLER) algorithm.[22]

C. Behavior of the precursory powders in ICTP flows

The precursory powders, which are assemblies of single particles, are injected with the carrier gas and vaporized in the plasma. The vapor is transported with the plasma flow and is then converted into nanoparticles in the cooling region. Therefore, the behavior of the powders and the vapor production by evaporation can be precisely determined through simultaneous computation of the trajectory and the temperature history accompanied by melting and evaporation. To model the behavior, several assumptions are introduced: (i) spherical particle; (ii) only drag force acting on each particle; (iii) evaporation temperature that is identical to the boiling point; (iv) uniform temperature distribution in the particle because of a low Biot number; (v) neither momentum transfer nor heat transfer from the precursory powders to plasma in the dilute loading; (vi) negligible transport property variation of the plasma by the vapor from the precursory powders.

The motion of a single precursory particle is described as

$$m_p\frac{d\boldsymbol{u}_p}{dt} = \frac{\pi}{8}d_p^2\rho C_D(\boldsymbol{u}-\boldsymbol{u}_p)|\boldsymbol{u}-\boldsymbol{u}_p| + m_p\boldsymbol{g}, \tag{13}$$

where m is the mass, t is the time, d is the diameter, and C_D is the drag force coefficient. Furthermore, $\boldsymbol{u}$ and $\boldsymbol{g}$ signify the vectors of the velocity and the gravitational force. Subscript p denotes particle. The dominant forces acting on the particle are the drag force from the plasma flow and the gravitational force. The added mass term and the Basset history term are negligible under these operating conditions because of the small particle size and the large density difference between the particles and the plasma.

The drag coefficient C_D is proposed in Ref. 23 as the following:

$$C_D = C_{Df}f_1f_2, \tag{14}$$

$$C_{Df} = \begin{cases} \dfrac{24}{\mathrm{Re}_{pf}} & (\mathrm{Re}_{pf} < 0.2) \\ \dfrac{24}{\mathrm{Re}_{pf}}\left(1+\dfrac{3}{16}\mathrm{Re}_{pf}\right) & (0.2 < \mathrm{Re}_{pf} < 2.0) \\ \dfrac{24}{\mathrm{Re}_{pf}}(1+0.11\mathrm{Re}_{pf}^{0.81}) & (2.0 < \mathrm{Re}_{pf} < 21.0) \\ \dfrac{24}{\mathrm{Re}_{pf}}(1+0.189\mathrm{Re}_{pf}^{0.62}) & (21.0 < \mathrm{Re}_{pf} < 200.0). \end{cases} \tag{15}$$

Therein, Re_p is the particle Reynolds number, defined as

$$\mathrm{Re}_p = \frac{d_p\rho}{\eta}|\boldsymbol{u}-\boldsymbol{u}_p|. \tag{16}$$

Because of the large temperature difference between the particle surface and the plasma bulk, these values are calculated on the film temperature defined as[24]

$$T_f = \tfrac{1}{2}(T_s + T_\infty), \tag{17}$$

where T represents the temperature. Subscripts f, s, and ∞, respectively, signify the film, surface, and bulk.

The drag coefficient is expected to be corrected using the term f_1, expressing the variation of the transport properties in the particle boundary layer, and the term f_2, expressing the noncontinuum effect on the particle with small size comparable to the mean free path of plasma,[24]

$$f_1 = \left(\frac{\rho_\infty\eta_\infty}{\rho_s\eta_s}\right)^{-0.45}, \tag{18}$$

$$f_2 = \left\{ 1 + \left(\frac{2-a}{a} \right) \left(\frac{\gamma}{1+\gamma} \right) \frac{4}{\mathrm{Pr}_s} \mathrm{Kn} \right\}^{-0.45} \quad (10^{-2} < \mathrm{Kn} < 1). \tag{19}$$

Therein, a is the thermal accommodation coefficient, γ is the specific heat ratio, and Pr is the Prandtl number; also, Kn represents the Knudsen number, which is defined as the ratio of the mean free path to the particle diameter.

During evaporation, the Knudsen number increases as the particle diameter decreases. With the large Knudsen number, the momentum transfer model based on the viewpoint of the continuum flow described above is no longer applicable. However, no useful formula is available to analyze this phenomenon under these conditions. For that reason, the model described above was applied even to the condition of $\mathrm{Kn} > 1$. The precursory powders were calculated to evaporate completely in a very short period after reaching the condition of $\mathrm{Kn} > 1$. Therefore, this approach is not an unreasonable one.[25]

The temperature evolution of the precursory particle is obtained by solving the energy balance equation. The total heat flux on the particle surface in the plasma $\dot{Q}_p$ is described using the heat transfer attributable to the plasma flow and the radiation loss as

$$\dot{Q}_p = \pi d_p^2 [\dot{q}_{\mathrm{plasma}} - \varepsilon_p \sigma_{\mathrm{SB}} (T_p^4 - T_a^4)], \tag{20}$$

where ε is the emissivity, σ_{SB} is the Stefan–Boltzmann constant, and T_a is the ambient temperature. Furthermore, $\dot{q}_{\mathrm{plasma}}$ represents the heat flux on a unit surface from the plasma.

$$\dot{q}_{\mathrm{plasma}} = h_{tf} (T - T_p). \tag{21}$$

In that equation, h_t is the heat transfer coefficient. On the other hand, $\dot{Q}_p$ can also be written for the particle temperature change and the phase changes such as melting and evaporation.

$$\dot{Q}_p = \begin{cases} \dfrac{\pi}{6} \rho_p d_p^3 c_p \dfrac{dT_p}{dt} & (T_p < T_m, T_m < T_p < T_b) \\ \dfrac{\pi}{6} \rho_p d_p^3 H_m \dfrac{dx}{dt} & (T_p = T_m) \\ -\dfrac{\pi}{2} \rho_p d_p^2 H_b \dfrac{dd_p}{dt} & (T_p = T_b). \end{cases} \tag{22}$$

Therein, c is the specific heat, H is the latent heat, and x is the molar fraction of liquid phase. Subscripts m and b, respectively, denote melting and boiling. The heat transfer coefficient h_t is given with the Nusselt number Nu,[26]

$$h_{tf} = \frac{\lambda_f}{d_p} \mathrm{Nu}_f f_3, \tag{23}$$

$$\mathrm{Nu}_f = (2 + 0.6 \mathrm{Re}_{pf}^{1/2} \mathrm{Pr}_f^{1/3}) \left(\frac{\rho_\infty \eta_\infty}{\rho_s \eta_s} \right)^{0.6} \left(\frac{C_{p_\infty}}{C_{p_s}} \right)^{0.38}. \tag{24}$$

The effect of the transport property variation in the particle boundary layer is taken into account in Eq. (24). Additionally, the heat transfer coefficient should be corrected using the term f_3, expressing the noncontinuum effect because of the small particle size.

$$f_3 = \left\{ 1 + \left(\frac{2-a}{a} \right) \left(\frac{\gamma}{1+\gamma} \right) \frac{4}{\mathrm{Pr}_s} \mathrm{Kn} \right\}^{-1} \quad (10^{-3} < \mathrm{Kn} < 1). \tag{25}$$

When the particle size becomes much smaller than the mean free path of the plasma through evaporation, the heat transfer should be considered in a free molecular flow regime.[27] In this regime, the heat flux from the plasma can be expressed according to each contribution of the plasma species,

$$\dot{q}_{\mathrm{plasma}} = \dot{q}_{\mathrm{Ar}} + \dot{q}_{\mathrm{Ar+}} + \dot{q}_{\mathrm{electron}}. \tag{26}$$

Subscripts Ar, Ar^+, and electron denote argon atoms, argon ions, and electrons. The heat fluxes attributable to them can be described as the following:

$$\dot{q}_{\mathrm{Ar}} = \frac{N_{\mathrm{Ar}} \bar{c}_{\mathrm{Ar}}}{4} a_{\mathrm{Ar}} (2k_B T - 2k_B T_p), \tag{27}$$

$$\dot{q}_{\mathrm{Ar+}} + \dot{q}_{\mathrm{electron}} = \frac{N_{\mathrm{Ar+}} \bar{c}_{\mathrm{Ar+}}}{4} [a_{\mathrm{Ar+}} (2k_B T - 2k_B T_p - e\phi_F) + a_{\mathrm{electron}} (2k_B T - 2k_B T_p) + E_I]. \tag{28}$$

In those expressions, N is the concentration, $\bar{c}$ is the first order mean thermal speed, k_B is the Boltzmann constant, e is the electric charge, ϕ_F is the floating potential, and E_I signifies the ionization energy. Equation (28) shows that the particle charge affects the heat transfer from the ions and electrons. The floating potential ϕ_F is expected to be determined as the following:

$$\phi_F = \frac{k_B T_{\mathrm{electron}}}{e} \ln \left(\frac{\bar{c}_{\mathrm{Ar+}}}{\bar{c}_{\mathrm{electron}}} \right) = \frac{k_B T_{\mathrm{electron}}}{2e} \ln \left(\frac{m_{\mathrm{electron}} T_{\mathrm{Ar+}}}{m_{\mathrm{Ar+}} T_{\mathrm{electron}}} \right). \tag{29}$$

In this study, the temperatures of argon atoms, argon ions, and electrons are equal.

A Gaussian size distribution with the average diameter of 10.0 μm and standard deviation of 3.0 μm was given for commercially available powders to the precursory powders of platinum. The powders were divided into 20 size bins, collectively accommodating 1.0–20.0 μm diameter particles, and supplied with the feed rate of 0.1 g min^{-1}. The properties of platinum such as its 2042 K melting point, its 4100 K boiling point, etc., were obtained from Ref. 28; the accommodation coefficients were obtained from Ref. 27.

The equations of the behavior of the precursory powders are solved with fourth-order Runge–Kutta–Gill method. The vapor production rate by evaporation is calculated in each control volume using the Particle Source In Cell (PSI-Cell)-like method[29] and used as the input data for Eq. (48), as described in the next section.

D. Nanoparticle formation

In the downstream region, the platinum vapor is quenched and converted into nanoparticles because the vapor pressure overcomes the saturation pressure. To describe this phenomenon, several assumptions are introduced: (i) spherical nanoparticles; (ii) negligible nanoparticle inertia; (iii) the identical velocity and temperature of nanoparticles as those of the gas flow; (iv) negligible heat generation caused by condensation; (v) negligible electric charge of nanoparticles; and (vi) nanoparticle size with a log-normal distribution. The particle size distribution functions (PSDFs) of nanoparticles at a certain time and position are obtainable by solving the general dynamic equation for an aerosol.[30]

$$\frac{\partial}{\partial t}n(v_p) = I \cdot \delta_D(v_p - v_p^*) - \frac{\partial}{\partial v_p}[Gn(v_p)] + \frac{1}{2}\int_0^{v_p} \beta(v_p', v_p - v_p')n(v_p')n(v_p - v_p')dv_p' - \int_0^{\infty} \beta(v_p, v_p')n(v_p)n(v_p')dv_p' - \nabla \cdot \boldsymbol{u}n(v_p) + \nabla \cdot D(v_p)\nabla n(v_p) - \nabla \cdot \boldsymbol{u}_{\mathrm{th}}(v_p)n(v_p). \quad (30)$$

In those equations, n is the PSDF, v is the volume, I is the homogeneous nucleation rate, δ_D is the Dirac delta function, G is the growth rate by heterogeneous condensation, β is the collision frequency function, and D is the diffusion coefficient. Superscript $*$ denotes the value in the critical state. Subscript th stands for thermophoresis. For the right-hand side of Eq. (30), the first and the second terms signify the generation of nuclei by homogeneous nucleation and growth by heterogeneous condensation, respectively. The set of the third and the fourth terms expresses growth by coagulation between nanoparticles. The fifth, sixth, and seventh terms, respectively, represent the mass transfer effects caused by convection, diffusion, and thermophoresis.

The homogeneous nucleation rate I is given by the self-consistent classical theory modified by Ref. 31,

$$I = \frac{\beta(v_{\mathrm{monomer}}, v_{\mathrm{monomer}})N_S^2 S}{12}\sqrt{\frac{\Theta}{2\pi}}\exp\left(\Theta - \frac{4\Theta^3}{27(\ln S)^2}\right), \quad (31)$$

in which the subscripts monomer and S, respectively, denote the monomers of the material and the saturated state. The supersaturation ratio S is defined using the vapor pressure and the saturation pressures,

$$S = \frac{p_{\mathrm{vapor}}}{p_S}. \quad (32)$$

Subscript vapor stands for the material vapor. The normalized surface tension Θ is defined with surface tension σ_{st},

$$\Theta = \frac{\sigma_{\mathrm{st}} s_{\mathrm{monomer}}}{k_B T}. \quad (33)$$

Homogeneous nucleation produces nuclei with a critical size because the nuclei smaller than the critical size are unstable and easily evaporate. The critical volume v_p^* is given in Ref. 30 as

$$v_p^* = \frac{\pi}{6}\left(\frac{4\sigma_{\mathrm{st}} v_{\mathrm{monomer}}}{k_B T \ln S}\right)^3. \quad (34)$$

The particle growth rate by heterogeneous condensation G is simply estimated using the bombardment of monomers on the nucleus' surface,

$$G = \frac{dv_p}{dt} = \frac{\pi d_p^2 v_{\mathrm{monomer}}(p_{\mathrm{vapor}} - p_S)}{(2\pi m_{\mathrm{monomer}} k_B T)^{1/2}}. \quad (35)$$

In a free molecular regime, the collision frequency function β between nanoparticles with volume v_p and v_p' is written as

$$\beta(v_p, v_p') = \left(\frac{3}{4\pi}\right)^{1/6}\left(\frac{6k_B T}{\rho_p}\right)^{1/2}\left(\frac{1}{v_p} + \frac{1}{v_p'}\right)^{1/2}(v_p^{1/3} + v_p'^{1/3})^2. \quad (36)$$

The diffusion coefficient D of the nanoparticles with the volume v_p is given similarly as proposed in Ref. 32,

$$D(v_p) = \frac{k_B T}{3\pi\eta}\left[\left(\frac{\pi}{6v_p}\right)^{1/3} + 3.314l\left(\frac{\pi}{6v_p}\right)^{2/3}\right]. \quad (37)$$

The mean free path l is estimated from

$$l = \frac{\eta}{\rho}\cdot\left(\frac{\pi m_{\mathrm{gas}}}{2k_B T}\right)^{1/2}, \quad (38)$$

where subscript gas denotes the bulk gas. In this study, the thermophoretic effect is also considered because the present nanoparticle formation process has a temperature field with a steep spatial gradient. Its velocity is induced on the nanoparticles. The thermophoretic velocity $\boldsymbol{u}_{\mathrm{th}}$ is given as

$$\boldsymbol{u}_{\mathrm{th}}(v_p) = -K_{\mathrm{th}}\frac{\eta}{\rho}\frac{\nabla T}{T}. \quad (39)$$

The coefficient K_{th} depends on the nanoparticle size, the thermal conductivity of the nanoparticles, and that of the gas,[33]

$$K_{\mathrm{th}} = \frac{2.34\left(\frac{\lambda}{\lambda_p} + 2.18\frac{l}{d_p}\right)\left\{1 + \frac{l}{d_p}\left[1.2 + 0.41\exp\left(-\frac{0.88d_p}{l}\right)\right]\right\}}{\left(1 + 3.42\frac{l}{d_p}\right)\left(1 + 2\frac{\lambda}{\lambda_p} + 4.36\frac{l}{d_p}\right)}. \quad (40)$$

It is generally difficult to solve Eq. (30) because of its nonlinearity. For that reason, several numerical methods to solve it have been proposed and applied to the plasma-aided nanoparticle formation processes.[2–4,8–10,15,25,34,35] For the present study, the method using the moments of the PSDF, the so-called moment method, is adopted because the spatial distribution of the growing nanoparticles with each size is obtainable even if the flow field has a negative velocity such as a counterflow or a circulating zone. The moment method handles the first three moments of the PSDF.

The kth moment M_k is defined as

$$M_k = \int_0^\infty v_p^k n(v_p) dv_p \quad (k = 0,1,2). \tag{41}$$

The zeroth moment and the first moment are, respectively, the total concentration and the total volume of the generated nanoparticles. The second moment is also known to be proportional to the total light scattering by the nanoparticles when they have much smaller size than the wavelength of the incident light. Consequently, Eq. (30) can be transformed into the simultaneous moment transport equations in a steady state as

$$\boldsymbol{u} \cdot \nabla M_k = [\dot{M}_k]_{\text{nucleation}} + [\dot{M}_k]_{\text{condensation}} + [\dot{M}_k]_{\text{coagulation}} + [\dot{M}_k]_{\text{diffusion}} + [\dot{M}_k]_{\text{thermophoresis}} (k = 0,1,2). \tag{42}$$

Therein, $[\dot{M}_k]$ expresses the net production rate of the kth moment. With the assumption (vi), these three equations are mathematically closed with the relation below among the moments, the geometric standard deviation σ_g, and the geometric mean volume v_g.

$$M_k = M_0 v_g^k \exp\left(\tfrac{9}{2} k^2 \ln^2 \sigma_g\right), \tag{43}$$

$$\ln^2 \sigma_g = \frac{1}{9} \ln\left(\frac{M_0 M_2}{M_1^2}\right), \tag{44}$$

$$v_g = \frac{M_1^2}{M_0^{3/2} M_1^{1/2}}. \tag{45}$$

Hence, the rates of change of the moments attributable to nucleation, condensation, and coagulation in Eq. (42) can be written as

$$[\dot{M}_k]_{\text{nucleation}} = I \cdot v_p^{*k} \quad (k = 0,1,2), \tag{46}$$

$$[\dot{M}_k]_{\text{condensation}} = \begin{cases} 0 & (k=0) \\ \xi_1 (S-1) M_{2/3} & (k=1) \\ 2\xi_1 (S-1) M_{5/3} & (k=2), \end{cases} \tag{47}$$

$$[\dot{M}_k]_{\text{coagulation}} = \begin{cases} -\xi_2 \zeta_0 (M_{2/3} M_{-1/2} + 2M_{1/3} M_{-1/6} + M_{1/6} M_0) & (k=0) \\ 0 & (k=1) \\ 2\xi_2 \zeta_2 (M_{5/3} M_{1/2} + 2M_{4/3} M_{5/6} + M_{7/6} M_1) & (k=2), \end{cases} \tag{48}$$

$$\xi_1 = v_{\text{monomer}} N_S (36\pi)^{1/3} \left(\frac{k_B T}{2\pi m_{\text{monomer}}}\right)^{1/2}, \quad \xi_2 = \left(\frac{3}{4\pi}\right)^{1/6} \left(\frac{6k_B T}{\rho_p}\right)^{1/2}, \tag{49}$$

$$\zeta_0 = 0.633 + 0.092\sigma_g^2 - 0.022\sigma_g^3, \quad \zeta_2 = 0.39 + 0.5\sigma_g - 0.214\sigma_g^2 + 0.029\sigma_g^3. \tag{50}$$

Heterogeneous condensation does not change the total concentration. Therefore, the rate of change of the zeroth moment, because of condensation, is zero. Through coagulation, the first moment does not change because the total volume is conserved. On this point, detailed discussion is presented in Ref. 36.

In association with Eq. (37), the diffusion term can be given as the following:

$$[\dot{M}_k]_{\text{diffusion}} = \nabla \cdot D_k \nabla M_k \quad (k = 0,1,2), \tag{51}$$

$$D_k = \begin{cases} \xi_3 v_g^{-1/3} \exp\left(\frac{1}{2} \ln^2 \sigma_g\right) + \xi_4 v_g^{-2/3} \exp(2 \ln^2 \sigma_g) & (k=0) \\ \xi_3 v_g^{-1/3} \exp\left(-\frac{5}{2} \ln^2 \sigma_g\right) + \xi_4 v_g^{-2/3} \exp(-4 \ln^2 \sigma_g) & (k=1) \\ \xi_3 v_g^{-1/3} \exp\left(-\frac{11}{2} \ln^2 \sigma_g\right) + \xi_4 v_g^{-2/3} \exp(-10 \ln^2 \sigma_g) & (k=2), \end{cases} \tag{52}$$

$$\xi_3 = \frac{k_B T}{3\pi\eta} \cdot \left(\frac{\pi}{6}\right)^{1/3}, \quad \xi_4 = \frac{k_B T}{3\pi\eta} \cdot 3.314l \cdot \left(\frac{\pi}{6}\right)^{2/3}. \tag{53}$$

The rate of change of the moments attributable to thermophoresis is written simply as

$$[\dot{M}_k]_{\text{thermophoresis}} = -\nabla \cdot \left(K_{\text{th}} \frac{\eta}{\rho} \nabla \ln T \cdot M_k\right) \quad (k = 0,1,2). \tag{54}$$

In this scheme, individual nanoparticles are not pursued because each of the three moments is solved and connected with the others by Eqs. (43)–(45). Therefore, the coefficient of thermophoretic effect described by Eq. (40) is estimated by replacing d_p with the volume mean diameter $\langle d_p \rangle_v$ given below.

$$\langle d_p \rangle_v = \left(\frac{6M_1}{\pi M_0}\right)^{1/3}. \tag{55}$$

In addition, the platinum vapor concentration must be solved simultaneously. The conservation equation of the vapor is written as follows:

$$\boldsymbol{u} \cdot \nabla N_{\text{vapor}} = \nabla \cdot (D_{\text{vapor}} \nabla N_{\text{vapor}}) + \dot{N}_{\text{vapor}}. \tag{56}$$

The net production rate of the platinum vapor $\dot{N}_{\text{vapor}}$ is estimated using contributions from evaporation, nucleation, and condensation, as

$$\dot{N}_{\text{vapor}} = [\dot{N}_{\text{vapor}}]_{\text{evaporation}} - I \cdot \frac{v_p^*}{v_{\text{monomer}}} - \frac{[\dot{M}_1]_{\text{condensation}}}{v_{\text{monomer}}}. \tag{57}$$

The production by evaporation is obtained from the computation of the precursory powder behavior, as explained in the previous section.

As the boundary conditions, the Neumann condition was given to each moment and the vapor concentration on the central axis and at the exit. Additionally, it was given to the vapor concentration at the wall. A certain amount of nanoparticles would be expected to be deposited on the wall. However, the exact consideration of this phenomenon deviates from the objective of this paper. For that reason, the value of zero was set for the moments at the wall for simplicity, which means that all the nanoparticles deposit on the wall.

As explained earlier, the properties of platinum were obtained from Ref. 28 and the diffusion coefficient of the vapor was calculated from the formula proposed in Ref. 20.

The computational domain was rediscretized into the finer nonuniform grid system of 707 and 47 in the axial and radial directions, respectively, to capture the homogeneous nucleation more precisely. The information related to the thermofluid field and the vapor concentration obtained from the prior computations was interpolated. The equations of the moments and the vapor concentration were solved using a SIMPLE-like algorithm.

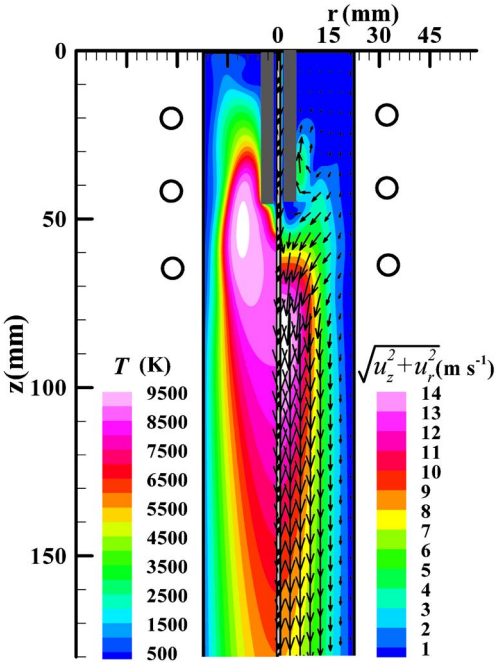

FIG. 2. (Color online) Thermofluid field in the plasma torch region of case A: temperature (left) and velocity (right).

III. RESULTS AND DISCUSSION

A. Thermofluid fields in the ICTP flows

Figure 2 shows the temperature and velocity fields of case A in the plasma torch (z=0–180 mm), which is the upstream region from the cooling region at z=200 mm. In the left side of Fig. 2, the intensively high-temperature zone is generated near the coil region, where argon gas partially ionizes and where many electrons are produced. That high-temperature zone has a large electrical conductivity. Because the electric field is induced near the coil region, the flow is Joule heated, as expressed by Eq. (8), which maintains the ICTP flow.[37] In the present study, the water-cooled nozzle for powder injection is assumed to be made of copper with electrical conductivity (5.81×10^7 S m^{-1}) that is much greater than that of the present argon plasma (2.70×10^3 S m^{-1}), which might enhance the Joule heating. However, this computation has shown no remarkable influence of this electrical conductive nozzle on the thermofluid field. The "skin effect" is observed by which the electromagnetic waves from the external coil current cannot penetrate to the plasma's central region. The same result has also been reported in a previous study (Ref. 38).

The right side of Fig. 2 presents the velocity fields in the plasma torch region with the velocity vectors and the contours of the velocity magnitude without the azimuthal component. In the coil region, Lorentz force attributable to the induced electromagnetic field pinches the plasma flow, which produces a recirculation zone in the upper coil region. This recirculation zone has prevented powder injection. Therefore, the injection nozzle has been introduced to overcome this problem. In the downstream region from the coils, the flow has a large velocity zone because of the pinch effect by

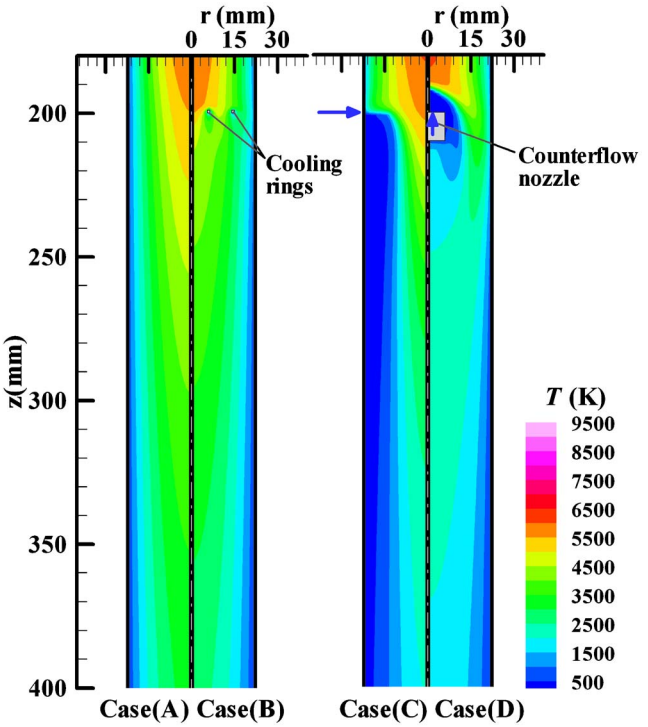

FIG. 3. (Color online) Temperature fields in the cooling region.

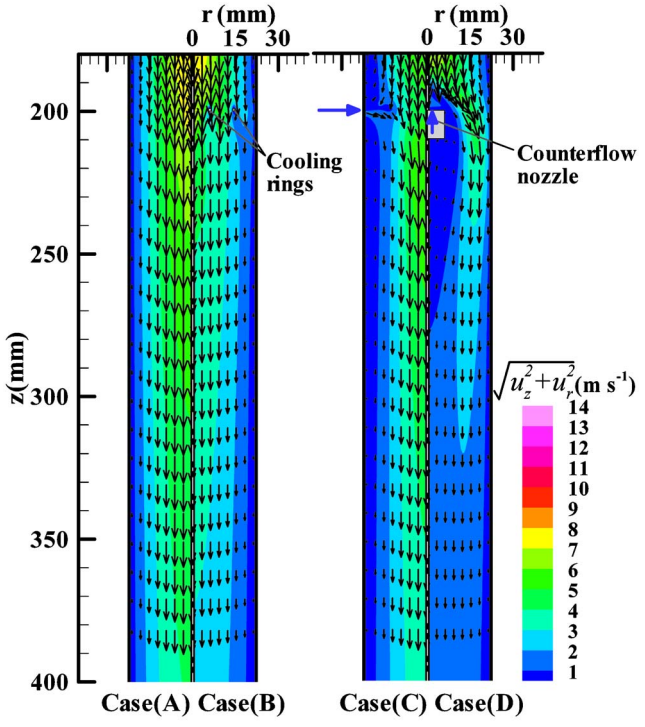

FIG. 4. (Color online) Velocity fields in the cooling region.

the Lorentz force as well as the drastic thermal expansion. Cases B, C, and D show almost identical profiles in their thermofluid fields.

Figure 3 shows the temperature fields in the cooling region of the four cases. In case A, without any cooling portion, the flow has a low temperature layer only near the water-cooled wall. In case B, the flow temperature decreases to around 3000 K because of the cooling rings. In case C, the radial cooling gas injection quenches the flow and the temperature decreases drastically. The flow with the low temperature near the wall is cooled. In case D, the flow with the higher temperature near the central axis is drastically cooled. Its radial temperature profile in the downstream region is more uniform than that of case C, which will cause a notable difference of the nanoparticle distributions. In both cases C and D, substantial nanoparticle formation is expected because a more intensive homogeneous nucleation will occur at a zone with a steeper temperature gradient.[6]

Figure 4 depicts the velocity fields in the cooling region with the velocity vectors and the contours of the velocity magnitude without the azimuthal component. In cases B–D, the flows slow at the low temperature zones because the thermally expanded flows cool rapidly and their density increases, which satisfies the mass conservation of Eq. (1). In case D, the negative velocity zones are found in the counterflow itself and the circulation behind the nozzle, which has rendered numerical analyses of nanoparticle formation difficult. Nevertheless, this "moment method" can overcome this problem, as described later.

B. Behavior of the precursory powders

Figures 5(a) and 6(b), respectively, portray the histories of the precursory particle temperature and diameter. As a representative example, the results obtained for a platinum particle with the average diameter of $d_p=10$ μm are presented. In all cases, the temperatures increase rapidly and reach the boiling point via the melting point; subsequently, the particles shrink by evaporation. As a result, the particles are completely vaporized near $z=69$ mm, although slight differences among the four cases are observed. Numerical results show that they are vaporized completely in the plasma as well when the particles have even the larger diameter such as $d_p=20$ μm.

Concerning the precursory particle velocity, a similar result to that described in Ref. 25 is obtained. The particle flies

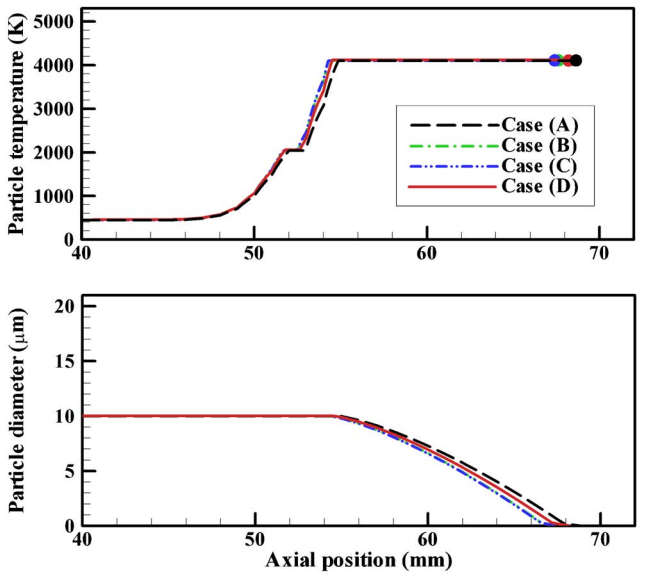

FIG. 5. (Color online) Behavior of the precursory platinum particles with $d_p=10$ μm: (a) particle temperature; (b) particle diameter.

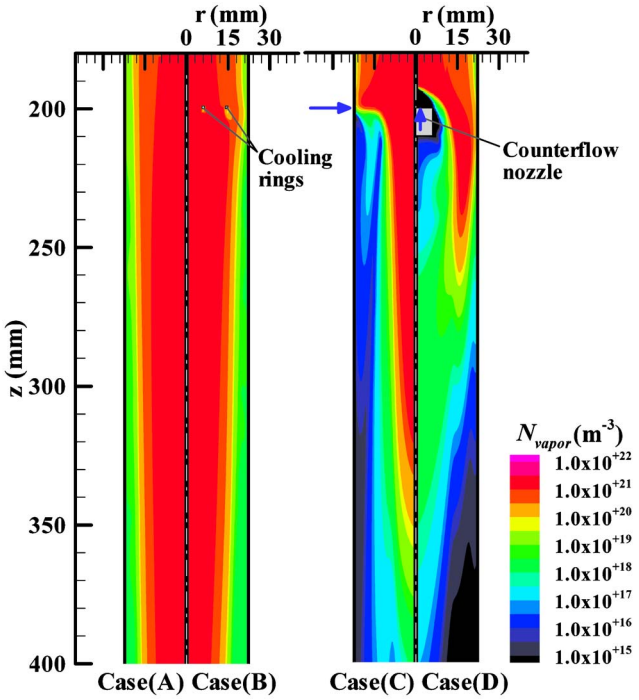

FIG. 6. (Color online) Concentration of vapor.

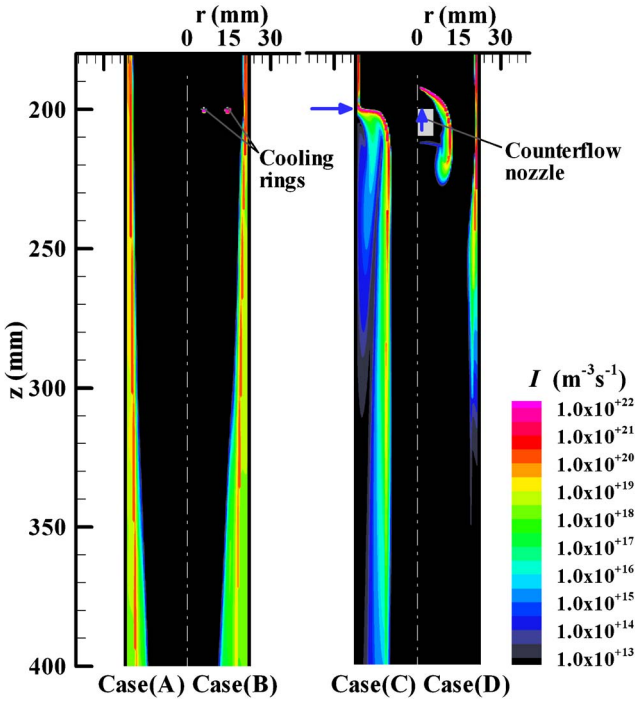

FIG. 7. (Color online) Homogeneous nucleation field.

along the central axis, being accelerated by the plasma flow. Immediately after the Knudsen number exceeds unity, the particle velocity drastically increases. A detailed discussion of that phenomenon is provided in Ref. 25.

C. Spatial distribution and the nanoparticle formation mechanism

Figure 6 shows the two-dimensional distributions of the platinum vapor concentration in the four cases. As shown in cases A and B, small amounts of the vapor are consumed near the wall. Although the vapor concentration seems to decrease at the cooling rings in case B, the vapor distributions have little difference between these two cases. On the other hand, with the cooling gas injections in cases C and D, the vapors drastically decrease through consumption resulting from conversion into nanoparticles.

Figure 7 presents the homogeneous nucleation fields in the cooling regions. These fields indicate the place in which nuclei of nanoparticles are generated. The generation of nuclei, or the so-called embryos, is observed near the wall in all cases because of the low temperature. In case B, local homogeneous nucleation also seems to occur at the cooling rings. In cases C and D, strong nucleation fields form, especially at the border between the high-temperature flow and the cooling gas. Particularly in case C, the nuclei are generated in a larger area than in case D. In addition, in these cases, the effect of the cooling gas injection is suppression of homogeneous nucleation near the wall, in contrast to the effects observed for cases A and B.

Figure 8 shows the two-dimensional distributions of the zeroth moment, which is equivalent to the total concentration of nanoparticles formed in the cooling regions. In case A, nanoparticles exist only near the wall, as predicted from the homogeneous nucleation field in Fig. 7. Observations reveal that the nanoparticles somewhat diffuse to the central axis. However, they disappear in the high-temperature zone, where they evaporate. In case B, nanoparticles seem to be generated around the cooling rings. However, they are convectively transported downstream into the high-temperature zone, where they disappear because of evaporation. In cases C and D, the cooling gas injection dramatically promotes nanoparticle generation. Consequently, nanoparticles are distributed throughout the downstream region. The nanopar-

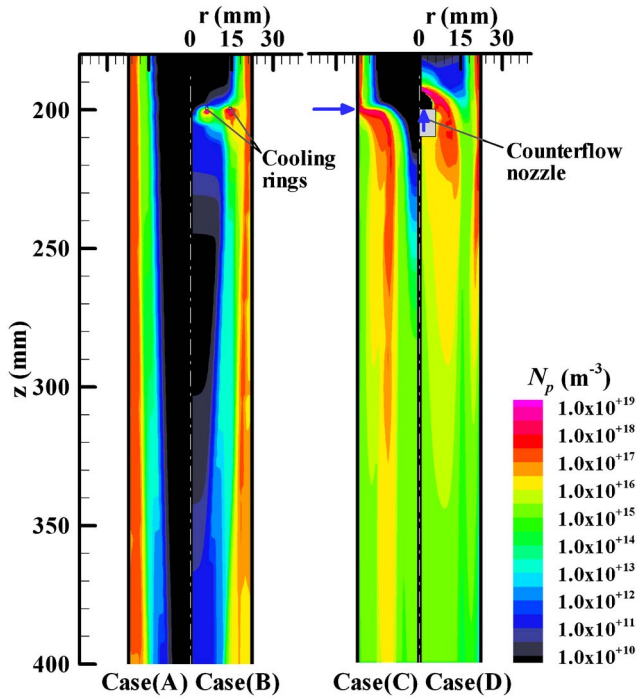

FIG. 8. (Color online) Total concentration of nanoparticles.

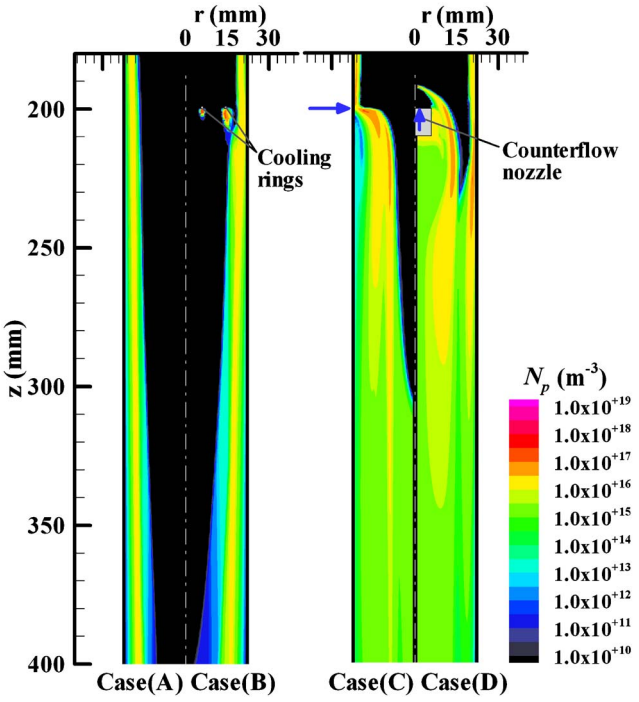

FIG. 9. (Color online) Total concentration of nanoparticles with $d_p > 5$ nm.

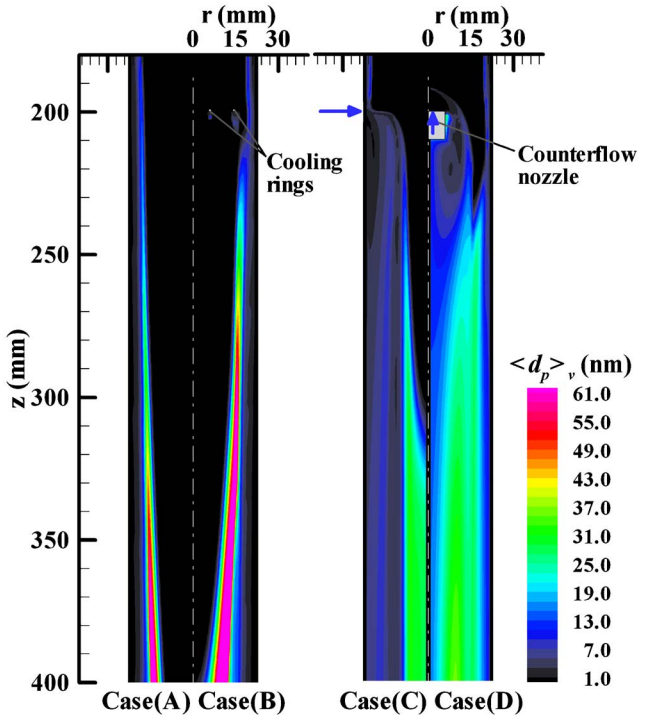

FIG. 10. (Color online) Volume mean diameter.

ticles gradually decrease as they are transported downstream because they concomitantly grow by coagulation with the decrease in their number. Figure 7 shows that homogeneous nucleation continues to occur even in the downstream region ($11 < r < 12$ mm) in case C. Therefore, many nanoparticles including nuclei are found there. Contrasted to this case, the distribution in case D is uniform in the radial direction.

As mentioned above, it is noteworthy that the zeroth moment includes tiny nuclei, which cannot actually be regarded as "particles." Even if the nuclei are considered as particles, particles with $d_p < 5$ nm are only slightly detected by experimental equipment such as a scanning mobility particle sizer.[39] Therefore, the total concentration of the particles with $d_p > 5$ nm is presented in Fig. 9 as the distribution of "nanoparticles." A comparison of Figs. 8 and 9 gives information related to the generation of the nuclei and their growth to nanoparticles. For instance, results show that almost all the nanoparticles in the zones of $N_p > 1.0 \times 10^{17}$ in Fig. 8 are immature nanoparticles with $d_p < 5$ nm. In addition, the distributions of the volume mean diameters are presented in Fig. 10 to elucidate the growth mechanism of the platinum nanoparticles for each cooling system.

In case B, the remarkably large volume mean diameter over 60 nm is obtained in $8 < r < 13$ mm of the downstream region in Fig. 10, but only a few nanoparticles exist there, as shown in Fig. 9. The nanoparticles in the high concentration zone seem to have small sizes of, at most, 10 nm. At $z > 320$ mm in case C, even though no difference of the total concentrations of the nanoparticles with $d_p > 5$ nm is seen between $0 < r < 8$ mm and $10 < r < 20$ mm in Fig. 9. The nanoparticles in $0 < r < 8$ mm and in $10 < r < 20$ mm have volume mean diameters of around 30 and 8 nm, respectively, as depicted in Fig. 10. The nanoparticles near the central axis can grow because the gas there includes an abundance of platinum vapor, as depicted in Fig. 6, whereas the gas in the outer zone has little vapor to support the growth of nanoparticles. Furthermore, the concentration of the nanoparticles does not change in $0 < r < 8$ mm of $z > 320$ mm in Fig. 9, which shows that the dominant process of the nanoparticle growth there is heterogeneous condensation. In case D, the nanoparticles near the side of the counterflow nozzle and those near the wall merge around $z = 250$ mm and $r = 17$ mm, which results in growth by coagulation. Figure 10 shows that the nanoparticles in the zone of $250 < z < 320$ mm grow rapidly by heterogeneous condensation with drastic vapor consumption, as depicted in Fig. 6. Simultaneously, coagulation growth continues with the gradual decrease in the number of nanoparticles to the downstream region. The nanoparticles produced by this cooling system therefore seem to have a uniform distribution of the volume mean diameter. These results described above imply that more numerous smaller nanoparticles are producible with cooling gas injections in cases C and D than in cases A and B. Moreover, it is also indicated that this model is a useful tool for application to this kind of problem, which even includes counterflows or circulating flows.

For better understanding, the radial distributions of the total concentrations and the volume mean diameters are presented, respectively, in Figs. 11 and 12. It is noteworthy that these profiles are extracted from Figs. 8 and 10. In cases A and B, the concentrations in $13 < r < 15$ mm increase as transported from $z = 300$ mm to $z = 400$ mm because of homogeneous nucleation and the radial diffusion from the near-wall zone, as presented in Fig. 11. Even though the volume mean diameters there decrease because of nucleation, the nanoparticles which have already existed are presumed to grow by heterogeneous condensation and radially diffuse toward the central axis. Consequently, Fig. 12(b) shows the

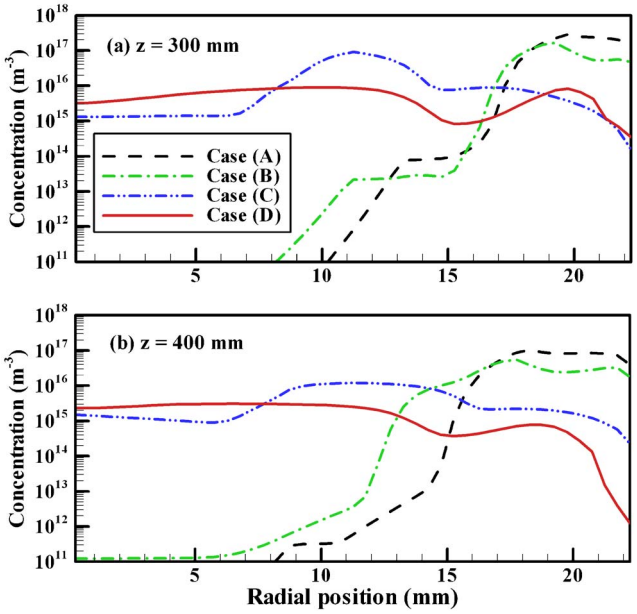

FIG. 11. (Color online) Radial distribution of nanoparticle concentration at (a) $z=300$ mm and (b) $z=400$ mm.

remarkably large diameter of about 100 nm around $r=11$ mm, especially in case B. Because of a high temperature in this zone, the evaporation effect is large and the large critical size is required for nanoparticles to exist stably, as given as Eq. (34). Therefore, the nanoparticles there decrease as presented in Fig. 11(b). In cases C and D, the radial profiles of the concentrations are more uniform; moreover, this tendency is sustained. As presented in Fig. 12(b), the volume mean diameter around 30 nm is consequently obtained only in $0<r<7$ mm in case C, although the most uniform radial profile of the volume mean diameter from 15 to 30 nm is obtainable in case D. Therefore, it might be concluded that

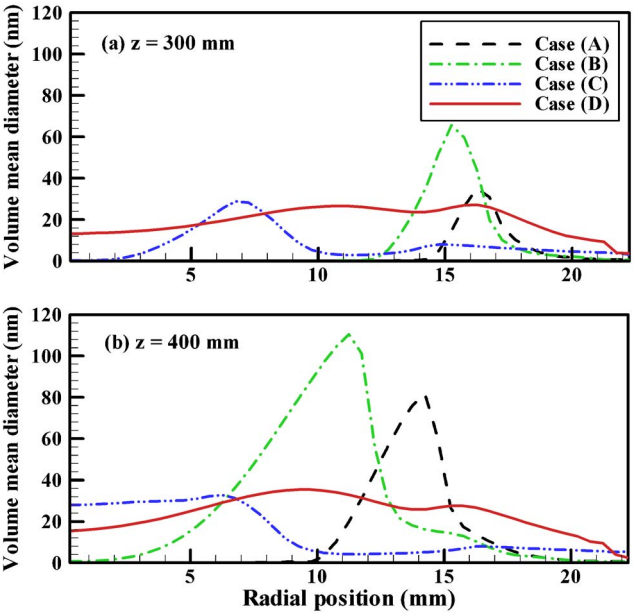

FIG. 12. (Color online) Radial distribution of volume mean diameter at (a) $z=300$ mm and (b) $z=400$ mm.

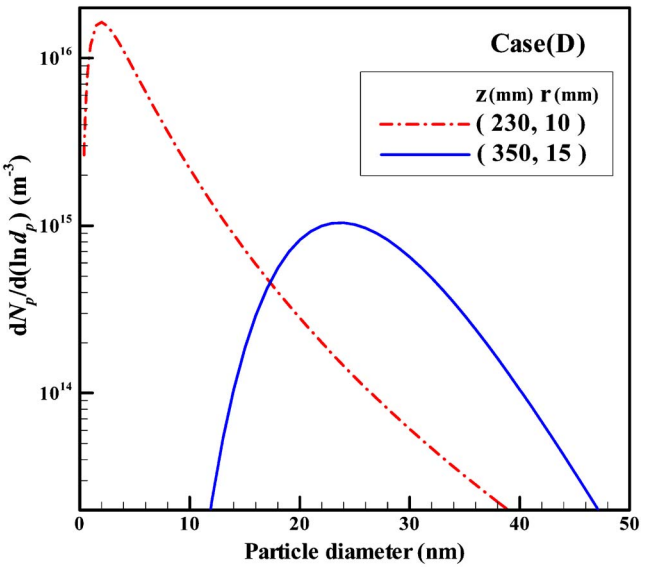

FIG. 13. (Color online) Particle size distributions in case D.

the counterflow cooling system is most useful to produce nanoparticles that must be produced to a uniform size.

It is important to recognize that the entire preceding discussion has been premised on the particles' number and mean diameter. Nanoparticles indeed have dispersion in their sizes. To investigate this problem, this moment method is a powerful scheme because it gives information related to the particle size distribution with the dispersion as well as the mean diameter at arbitrary positions. As representatives, the PSDFs at the two positions in case D are presented in Fig. 13. The longitudinal axis shows another expression of PSDFs estimated from the basic PSDF $n(v_p)$ of this model. This expression is based on the particle diameter d_p. Therefore, it is perhaps easier to understand than the expression based on the particle volume v_p. At $z=230$ mm and $r=10$ mm near the counterflow nozzle, the PSDF has a peak at $d_p=2$ nm because of many immature nanoparticles that are immediately present after homogeneous nucleation, as portrayed in Fig. 7. Nevertheless, nanoparticles larger than 10 nm are also mixed at the position. On the other hand, at $z=350$ mm and $r=15$ mm, the PSDF has a peak at $d_p=24$ nm and almost all the nanoparticle diameters are 12–47 nm after their growth by heterogeneous condensation and coagulation among themselves.

This model has another advantage of clarifying the spatial distribution of the nanoparticles with a specific size range, not only statistically but also directly, so that the evolution of the nanoparticle size is visible. For example, Figs. 14 and 15, respectively, show concentrations of the nanoparticles with the diameters of around 10 nm ($9.5<d_p<10.5$ nm) and around 20 nm ($19.5<d_p<20.5$ nm). Nanoparticles with diameters smaller than 20 nm tend to agglomerate easily. Therefore, the effective suppression of the agglomeration has been required for industrial applications. In particular, platinum nanoparticles around 10 nm have been used for purification of automobile exhaust gases as catalysts. In cases A and B, many nanoparticles around 10 nm are found near the wall, whereas nanoparticles around 20 nm

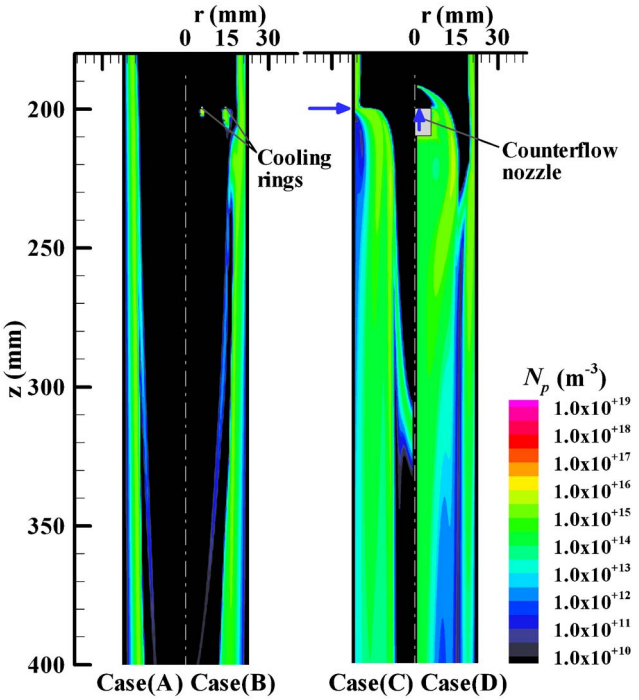

FIG. 14. (Color online) Concentration of nanoparticles with $d_p = 10 \pm 0.5$ nm.

exist closer to the central axis. This comparison between Figs. 14 and 15 illustrates that smaller nanoparticles near the wall diffuse toward the axis along with their increase in size. In case C, the nanoparticles around 10 nm are found in the near-axis zone of $310 < z < 340$ mm, but they immediately disappear in $z > 340$ mm, as presented in Fig. 14. The nanoparticles around 20 nm show up in the near-axis zone of $z > 320$ mm in Fig. 15. Consequently, the nanoparticles

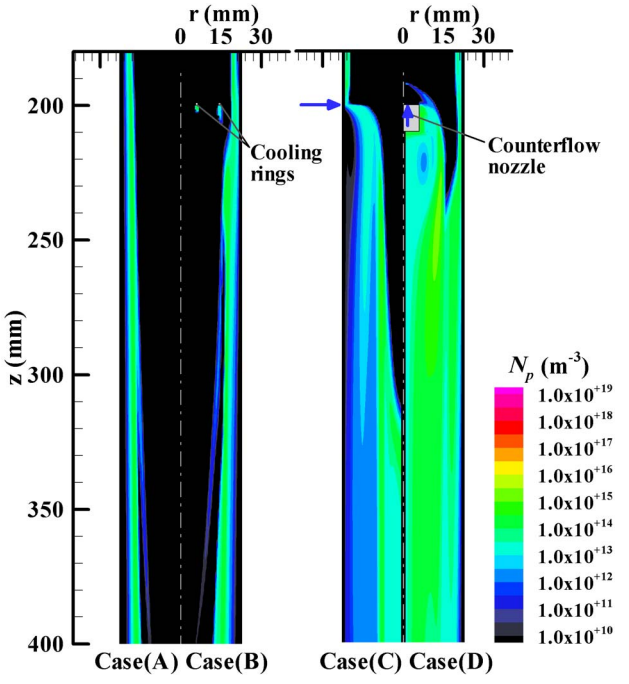

FIG. 15. (Color online) Concentration of nanoparticles with $d_p = 20 \pm 0.5$ nm.

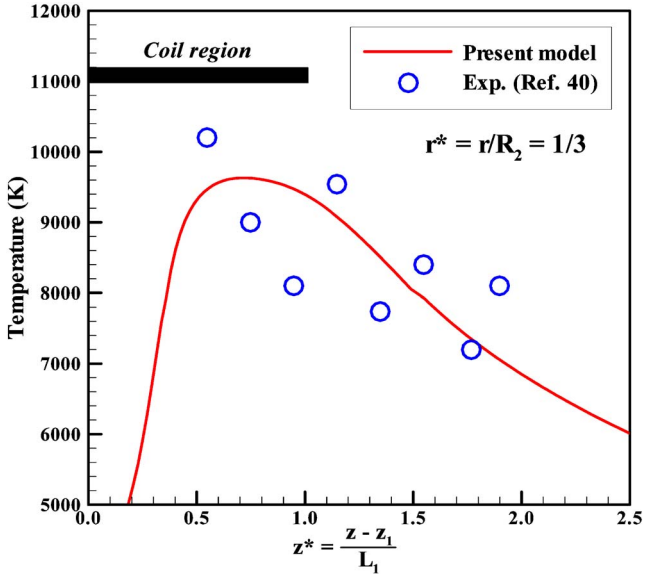

FIG. 16. (Color online) Validation of the present ICTP model by comparison with experiment results (Ref. 40).

around 10 nm appear in a short period and promptly grow up into those around 20 nm in the near-axis zone. Furthermore, because their number decreases in $z > 350$ mm, they seem to keep growing into larger nanoparticles. In case D, it is readily apparent that many nanoparticles of approximately 10 nm exist in the upstream zone, although many nanoparticles around 20 nm are found in the downstream zone of the cooling region, which helps us to elucidate the nanoparticle growth in this cooling system. In addition, the nanoparticles around 20 nm show the most uniform distribution of all the other cases.

IV. VALIDATION OF THE PRESENT MODEL

This model has clarified the heat and mass transfer processes in the platinum nanoparticle synthesis systems consisting of ICTPs associated with several cooling portions. To confirm its validity, the results obtained from this model should be compared to experimental evidence. However, experimental information for similar cases to this study is quite insufficient because plasmas naturally have very complicated fields and the nanoparticle formation progresses only in an overly short period, which makes it difficult to precisely measure. Therefore, this model is only roughly validated using a few available experimental data.

The plasma temperature profile obtained from the present ICTP model is presented in Fig. 16 with results from experimental measurements.[40] The coordinates are nondimensionalized for comparison in scale. Although the experimental data scatter somewhat because of the inclusion of errors, these results show good quantitative agreement. Unfortunately, no experimental result of platinum nanoparticles has been available. For that reason, iron nanoparticle formation in case A was computed under the same operating conditions as those of the experiment[41] to verify this nanoparticle formation model, as presented in Fig. 17. These results show qualitative agreement. The computational result presents a larger number of small nanoparticles than the experi-

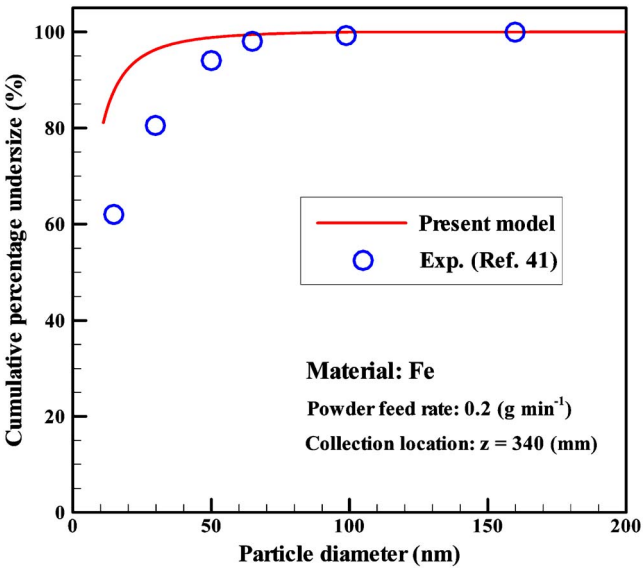

FIG. 17. (Color online) Validation of this nanoparticle formation model by comparison with experiment results (Ref. 41).

mental result. Actual experiments show many uncertain factors such as instability of plasma or turbulence of flow, which might engender a dispersed size distribution. Moreover, because nanoparticles tend to form their agglomerates, they might show a larger size distribution. Therefore, it can be concluded that this model expresses phenomena in the nanoparticle synthesis systems by ICTPs well to some extent. Moreover, it can be a useful tool for numerical prediction of this processing.

The model remains imperfect because it has been constructed on the assumption of a laminar flow. As described above, actual processes are considered to progress in a turbulent state, even though they have small Reynolds numbers. A plasma flow usually fluctuates. In addition, the edge of the plasma and the border with the cooling gas create intense shear layers with a large velocity difference and a steep temperature gradient, where many nuclei are generated, as shown in the preceding chapter. These shear layers are well known to easily roll up vortices. The larger-scale vortices induce smaller-scale vortices in sequence. Therefore, the flow field around these shear layers is capable of forming a hierarchical structure of multiscale vortices that complexly mix the plasma and the cool gas. An additional model should be combined with the present ICTP model as well as the higher spatial resolution to capture this turbulent-thermofluid mechanical phenomenon with accuracy. Reynolds averaging Navier–Stokes such as the k-ε model can be useful as a model expressing turbulence effects. In addition, large eddy simulation is considered as a powerful model because this phenomenon involves the complicated interaction between the vortical flow structure and the temperature field with a steep gradient. The growth mechanism of nanoparticles might be strongly affected because the effects of mixing and diffusion are enhanced in turbulence. The assumption of a laminar flow is ideal and might cause underestimation of a particle size. Moreover, the effect of heat generation caused by condensation is neglected in this model, which might also be a cause of the difference between the computational result and the experimental result. The generated heat is fed back to the flow, where it can change the temperature field and the thermodynamical characteristics, which are sensitive parameters for nanoparticle formation. Additionally, nanoparticles can be electrically charged by the influence of plasma, which would affect their own growth. Moreover, a log-normal PSD was assumed in the nanoparticle formation regime. This assumption is usually valid for mature nanoparticles which have grown through coagulation.[30] However, a PSD is also known to be able to deviate from a log-normal distribution or have a multimodal distribution at the early stage of formation.[10] This might be a cause of the discrepancy as well. Therefore, the present model demands improvement for better accuracy, although it is quite applicable to qualitative evaluation of nanoparticle synthesis by ICTP systems.

V. CONCLUDING REMARKS

A mathematical model was developed to simulate the comprehensive systems for platinum nanoparticle synthesis using an argon ICTP flow with forced cooling portions. Numerical investigation using the model was conducted to clarify and discuss the effects of the cooling methods on the formation mechanisms of the nanoparticles in distinctive thermofluid fields with strong two dimensionality. The following conclusions were obtained from results of this study.

(1) Nanoparticles are apparently generated around the cooling rings, but they rapidly disappear in the high-temperature zone when the cooling rings are installed. Nanoparticles are generated near the wall as well. They grow into large particles with volume mean diameter of more than 60 nm.
(2) Radial cooling gas injection, which engenders the intensive two dimensionality of the nanoparticle spatial distribution, strongly promotes nanoparticle formation. Only the nanoparticles near the central axis can grow by heterogeneous condensation because of the abundance of the platinum vapor.
(3) The counterflow cooling excellently promotes nanoparticle formation. Numerous generated nuclei grow by heterogeneous condensation with rapid vapor consumption and steady coagulation. Consequently, the nanoparticles produced by this cooling method obtain the most uniform radial profile of the concentration with volume mean diameter from 15 to 30 nm. The counterflow cooling system is most adequate to produce nanoparticles which must have uniform size.
(4.) Although the systems have strong two dimensionality with counterflows or circulating flows, this model is a useful tool for numerical prediction and evaluation of nanoparticle formation.

ACKNOWLEDGMENTS

This work was supported in part by Japan Society for the Promotion of Science. The authors gratefully acknowledge Dr. S. L. Girshick of the University of Minnesota for helpful advice on modeling.

[1]R. W. Siegel, Mater. Sci. Eng., A **168**, 189 (1993).
[2]S. L. Girshick, C.-P. Chiu, R. Muno, C. Y. Wu, L. Yang, S. K. Singh, and P. H. McMurry, J. Aerosol Sci. **24**, 364 (1993).
[3]J. F. Bilodeau and P. Proulx, Aerosol Sci. Technol. **24**, 175 (1996).
[4]M. Desilets, J. F. Bilodeau, and P. Proulx, J. Phys. D **30**, 1951 (1997).
[5]T. Watanabe and K. Fujiwara, Chem. Eng. Commun. **191**, 1343 (2004).
[6]M. Shigeta, T. Watanabe, and H. Nishiyama, Thin Solid Films **457**, 192 (2004).
[7]T. Watanabe, A. Nezu, Y. Abe, Y. Ishii, and K. Adachi, Thin Solid Films **435**, 27 (2003).
[8]M. Shigeta and T. Watanabe, JSME Int. J., Ser. B **48**, 425 (2005).
[9]M. Shigeta and H. Nishiyama, Trans. ASME, Ser. C: J. Heat Transfer **127**, 1222 (2005).
[10]M. Shigeta and T. Watanabe, J. Phys. D **40**, 2407 (2007).
[11]X. H. Wang, J.-G. Li, H. Kamiyama, M. Katada, N. Ohashi, Y. Moriyoshi, and T. Ishigaki, J. Am. Chem. Soc. **127**, 10982 (2005).
[12]T. Watanabe and H. Okumiya, Sci. Technol. Adv. Mater. **5**, 639 (2004).
[13]P. C. Kong and Y. C. Lau, Pure Appl. Chem. **62**, 1809 (1990).
[14]M. Ikeda, J.-G. Li, R. Ye, N. Kobayashi, Y. Moriyoshi, and T. Ishigaki, 18th International Symposium of Plasma Chemistry, 2007 (unpublished).
[15]M. Shigeta and T. Watanabe, "Two-dimensional analysis of nanoparticle formation in induction thermal plasmas with counterflow cooling," Thin Solid Films (in press).
[16]A. M. Contreras, "Nanolithographic Fabrication and Heterogeneous Reaction Studies of Two-Dimensional Platinum Model Catalyst Systems," Ph.D. thesis, University of California, Berkeley, 2006.
[17]A. Wieckowski, C. G. Vayenas, and E. R. Savinova, *Catalysis and Electrocatalysis at Nanoparticle Surfaces* (Marcel Dekker, New York, 2003).
[18]J. Mostaghimi and M. I. Boulos, Plasma Chem. Plasma Process. **9**, 25 (1989).
[19]N. Atsuchi, M. Shigeta, and T. Watanabe, Int. J. Heat Mass Transfer **49**, 1073 (2006).
[20]J. O. Hirschfelder, C. F. Curtiss, and R. B. Bird, *Molecular Theory of Gases and Liquids* (Wiley, New York, 1964).
[21]R. C. Miller and R. I. Ayen, J. Appl. Phys. **40**, 5260 (1969).
[22]S. V. Patankar, *Numerical Fluid Flow and Heat Transfer* (Hemisphere, New York, 1980).
[23]M. I. Boulos, IEEE Trans. Plasma Sci. **PS-6**, 93 (1978).
[24]E. Pfender and Y. C. Lee, Plasma Chem. Plasma Process. **5**, 211 (1985).
[25]M. Shigeta and T. Watanabe, Thin Solid Films **515**, 4217 (2007).
[26]Y. C. Lee, Y. P. Chyou, and E. Pfender, Plasma Chem. Plasma Process. **5**, 391 (1985).
[27]T. Honda, T. Hayashi, and A. Kanzawa, Int. J. Heat Mass Transfer **24**, 1247 (1981).
[28]Japan Institute of Metals, *Metal Data Book* (Maruzen, Tokyo, 1993).
[29]C. T. Crowe, M. P. Sharma, and D. E. Stock, ASME Trans. J. Fluids Eng. **99**, 325 (1977).
[30]S. K. Friedlander, *Smoke, Dust and Haze, Fundamentals of Aerosol Dynamics*, 2nd ed. (Oxford University Press, New York, 2000).
[31]S. L. Girshick, C.-P. Chiu, and P. H. McMurry, Aerosol Sci. Technol. **13**, 465 (1990).
[32]G. M. Phanse and S. E. Pratsinis, Aerosol Sci. Technol. **11**, 100 (1989).
[33]L. Talbot, R. K. Cheng, R. W. Schefer, and D. R. Willis, J. Fluid Mech. **101**, 737 (1980).
[34]M. Shigeta and T. Watanabe, J. Mater. Res. **20**, 2801 (2005).
[35]A. C. Cruz and R. J. Munz, IEEE Trans. Plasma Sci. **25**, 1008 (1997).
[36]S. E. Pratsinis and K.-S. Kim, J. Aerosol Sci. **20**, 101 (1989).
[37]M. Shigeta, T. Sato, and H. Nishiyama, Int. J. Heat Mass Transfer **47**, 707 (2004).
[38]X. Chen and E. Pfender, Plasma Chem. Plasma Process. **11**, 103 (1991).
[39]J. Hafiz, X. Wang, R. Mukherjee, W. Mook, C. R. Perrey, J. Deneen, J. V. R. Heberlein, P. H. McMurry, W. W. Gerberich, C. B. Carter, and S. L. Girshick, Surf. Coat. Technol. **188–189**, 364 (2004).
[40]T. Watanabe, K. Yanase, T. Honda, and A. Kanzawa, J. Chem. Eng. Jpn. **23**, 389 (1990).
[41]T. Yoshida and K. Akashi, Trans. Jpn. Inst. Met. **22**, 371 (1981).